Isolas of localized structures and Raman–Kerr frequency combs in micro-structured resonators

M. Tlidi [a,*], M. Bataille-Gonzalez [b], M.G. Clerc [b], L. Bahloul [c,d], S. Coulibaly [e], B. Kostet [a], C. Castillo-Pinto [f], K. Panajotov [f,g]

[a] *Faculté des Sciences, Université libre de Bruxelles (ULB), Campus Plaine, 1050, Brussels, Belgium*
[b] *Departamento de Física and Millennium Institute for Research in Optics, Facultad de Ciencias Físicas y Matemáticas, Universidad de Chile, Casilla 487-3, 1050, Santiago, Chile*
[c] *Electronics Department, Institute of Science, University Center of Tipaza Morsli Abdallah, Ouade Merzouk, 4200, Tipaza, Algeria*
[d] *Laboratoire d'Instrumentation, University of Sciences and Technology Houari Boumediene (USTHB), Algeria*
[e] *Université de Lille, CNRS, UMR 8523-PhLAM-Physique des Lasers Atomes et Molécules, F-59000, Lille, France*
[f] *Brussels Photonics Team, Department of Applied Physics and Photonics (B-PHOT TONA), Vrije Universiteit Brussel, Pleinlaan 2, 1050, Brussels, Belgium*
[g] *Institute of Solid State Physics, Bulgarian Academy of Sciences, 72 Tzarigradsko Chaussee Blvd., 1784, Sofia, Bulgaria*

A B S T R A C T

We theoretically investigate the combined impact of the Kerr and stimulated Raman scattering effect on the formation of localized structures and frequency comb generation. We focus on the regime of traveling wave instability. We first perform a real-order parameter description by deriving a Swift–Hohenberg equation with nonlocal delayed feedback. Second, we characterize the motion of traveling wave periodic solutions by estimating their thresholds as well their speed. By using a numerical continuation method, we construct a bifurcation diagram showing the emergence of traveling wave periodic solutions, as well as bright and dark moving localized structures. Numerical simulations of the generalized Lugiato–Lefever equation confirm evidence of isolas of localized structures. More importantly, we show that the stimulated Raman scattering strongly impacts the dynamics of localized structures by creating isolas consisting of bright and dark localized structures, and by inducing a motion of these structures. Finally, we provide a geometrical interpretation of the formation of isola stacks based on dynamical systems theory.

1. Introduction

In the early 2000s, Hänsch and Hall introduced and developed the optical frequency combs, which are equally spaced coherent laser lines [1,2]. They were generated by microcavity resonators and used to count light cycles. Their realization using mode-locked lasers and dissipative solitons has revolutionized many fields of science and technology, such as high-precision spectroscopy, metrology, and photonic analog-to-digital conversion [3,4]. The so-called soliton frequency combs are associated with the formation of localized structures (LSs) of light, which maintain their shape during propagation, and they have been experimentally reported in optical microcavities [5,6]. Those frequency combs are the spectral content of the localized structures, often called dissipative solitons, which have been theoretically predicted in driven cavities [7,8]. Dissipative solitons have been reported in the conservative limit when the injection and losses are both small and under zero frequency detuning limit [9,10]. The link between the localized structure in (micro-)resonators and frequency combs has been established [11–14]. The dynamics of interacting LSs can cause the stabilization of bounded localized states when a periodic

forcing is applied [15–17], when taking into account fourth-order dispersions [18–21] or spatial filtering (or gain dispersion in the time domain) [22]. This is caused by Cherenkov radiation [23–27], i.e., the radiation of dispersive waves that are weakly decaying.

Considerable attention has been paid recently to the formation of frequency combs under the combined action of Kerr nonlinearity and stimulated Raman scattering (SRS) in optical resonators such as whispering gallery mode resonators [28,29]. Since the Raman gain bandwidth is large (it is around 10 THz for silica glass), the combined influence of Raman scattering and Kerr nonlinearity is frequently observed [30–35]. The effects of SRS and Kerr on the front dynamics leading to the stabilization of LSs have recently been studied [36–40] in normal dispersion materials. In this case, LSs have been observed in a domain far from the traveling wave instability. In this regime, it has been shown that the combined action of SRS and Kerr nonlinearity is at the origin of generation of moving bright LSs [36–40]. In the absence of the SRS effect, bright LSs are unstable. The mechanism leading to the formation of LSs with varying width results from the locking front connecting two coexisting continuous wave states [41–44]. Close to the critical point associated with optical bistability, the

---

* Corresponding author.
E-mail address: mtlidi@ulb.ac.be (M. Tlidi).
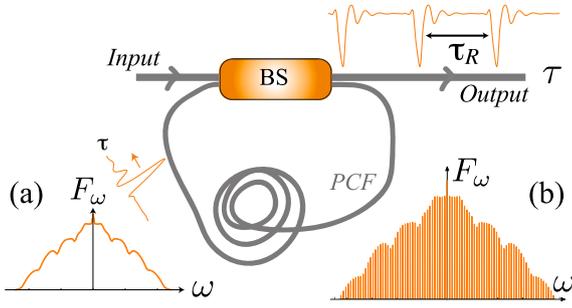
Fig. 1. Schematic setup of a ring cavity filled with a photonic crystal fiber (PCF). The cavity is driven by a coherent external injected beam. BS denotes a beam splitter and τ_R is the roundtrip time. (a) A single moving dark localized structure circulating within the cavity and its Fourier transform. (b) Frequency comb representing the Fourier transform of the train of dark localized structures coming out from the cavity.

interaction law between two well-separated fronts has been established analytically [37,39]. In many cases, properties of such localized states can be related to the phenomenon of collapsed snaking that has been found in the scalar Lugiato–Lefever equation (LLE [45]) with SRS [40] and without SRS [46,47], and in the vectorial case where polarization degree of freedom is considered [48,49].

The dispersion curve may be highly controlled using photonic crystal fibers. Such fibers play a significant role, especially traveling waves (TW) for supercontinuum generation [50–53]. When optical resonators are operating close to the zero dispersion wavelength, it is necessary to take into account higher-order dispersion. In silicon microring resonators, Kerr-Raman scattering and higher order dispersion have an impact on frequency comb formation [54–60]. In particular, complex dynamics characterized by the formation of dispersive waves, self-frequency-shifting, and frequency-locking have been reported [54].

In regimes devoid of traveling modulational instability, the impact of stimulated Raman scattering and the Kerr effect has been reported. In this case, bistability between CW solutions is necessary since the resulting LSs consist of an heteroclinic connection between the two branches of CW states [37,39]. Their bifurcation diagram follows a collapsed snaking type of bifurcation [40].

In this contribution, we theoretically investigate the homoclinic type of LSs in the regime where the system develops a traveling wave instability. Temporal LS can be formed even in the monostable regime. This type of solution has a homoclinic snaking type of bifurcation in the absence of SRS. We show that stimulated Raman scattering breaks the snaking structure and promotes LS branches in the form of isolas, which can form even in the monostable regime.

We show that when this instability becomes subcritical, the system develops a high degree of multistability: besides the continuous wave (CW), and the traveling periodic solutions, which are both stable, an additional variety of stable localized structures are generated. This behavior is independent of whether the system is operating in the monostable or the bistable regime. Using a continuation algorithm, we have established the bifurcation diagram associated with traveling waves. More importantly, we show that localized structures and combs branches of solution are isolas since they are not connected to any modulational instability or traveling wave thresholds.

The structure of the paper is as follows. We describe the creation of periodic TW solutions in the supercritical domain following the presentation of the Swift–Hohenberg equation with stimulated Raman scattering in Section 2. To characterize the motion, we estimate the threshold associated with the onset of motion as a function of injected field amplitude, as well as their speed. We show that when this instability becomes subcritical, the system develops a high degree of multistability: besides the continuous wave (CW), and the traveling periodic solutions, which are both stable, an additional variety of stable localized structures is generated. This behavior is independent of

whether the system is operating in the monostable or bistable regime. Then, in Section 3, we carry out a direct numerical simulation of dark and bright localized structures. We are able to create their bifurcation diagram, which provides proof of the existence of a stable single and multiple isolas, thanks to the continuation algorithm (see Subsection 3.1). In the last part of Subsection 3.2, we present numerical simulations showing that the generalized LLE supports isolas of temporal LSs. Section 4 discusses a geometrical interpretation of isola stack formation. Following the conclusions, we provide as an appendix a full derivation of the Swift–Hohenberg equation with nonlocal delayed feedback.

2. A derivation of a Swift–Hohenberg equation with stimulated Raman scattering

We consider a ring resonator filled-in with a Kerr dispersive medium such as a photonic crystal fiber (PCF). Fig. 1 shows a schematic of the PCF resonator. This resonator is coherently driven by a continuous wave monochromatic light with an electric field E_i and corresponding power E_i^2. Through the use of a beam splitter, the transmitted portion of this field is directed into the cavity and propagates through the PCF under the influence of dispersion, the Kerr effect, stimulated Raman scattering, and losses. During each round trip, the driving field and the light that moves throughout the resonator are coherently superimposed. High-order chromatic dispersion effects are crucial to the dynamics of this system when the PCF resonator is operating close to the zero dispersion wavelength. Taking into account these effects, the slowly varying envelope of the electric field within the resonator is described by the following generalized Lugiato–Lefever equation [55]

$$
\begin{aligned}
\frac{\partial E}{\partial \zeta} = {} & E_i - (1 + i\Delta)E + i\left(1 - f_r\right)|E|^2 E \\
& + i\beta_2 \frac{\partial^2 E}{\partial T^2} + i\beta_4 \frac{\partial^4 E}{\partial T^4} \\
& + i f_r E \int_{-\infty}^{T} \phi(T - T')|E(T')|^2 dT'.
\end{aligned}
\tag{1}
$$

where $E = E(\zeta, T)$ is the normalized mean-field cavity electric field, Δ accounts for the normalized detuning parameter, and losses are normalized to unity. The time ζ is the slow time describing the evolution over successive round trips, and T is the fast time in the reference frame moving with the group velocity of the light within the resonator. E_i is the input field amplitude. β_2 and β_4 are the second- and the fourth-order dispersion terms, respectively. The stimulated Raman scattering is described by the last term of Eq. (1) and by the cubic nonlinear term. The strength of the Raman is f_r. The kernel function is

$$
\phi(\tau) = a \exp\left(-\tau/\tau_2\right) \sin(\tau/\tau_1)
$$

with $a = \tau_0(\tau_1^2 + \tau_2^2)/(\tau_1 \tau_2^2)$, and $\tau_0 = [|\beta_4 L|/24\alpha]^{1/4}$, where α is the loss parameter, and L is the resonator length. The optical losses are determined by the mirror transmission and the intrinsic material absorption. The choice of this kernel, or influence function, shows an excellent agreement with experiments using standard fibers [61,62]. In the absence of the stimulated Raman scattering, i.e., $f_r = 0$, we recover the LLE with fourth-order dispersion [63]. In this case, Eq. (1) admits front-like states connecting the two continuous wave solutions (CWs) forming a bistable state [41], stationary LSs [18], and moving LSs due to the third-order dispersion effect [19,64–66].

We derive a paradigmatic Swift–Hohenberg equation (SHE) with stimulated Raman scattering describing the evolution of pulses propagating in a photonic crystal fiber resonator. This reduction is performed close to nascent optical bistability. Starting from the generalized LLE Eq. (1), the deviation u of the electric field from its value at the onset of bistability obeys a generalized SHE with stimulated Raman scattering

$$
\begin{aligned}
\partial_t u = {} & \eta + \mu u - u^3 + \beta \partial_\tau^2 u - \partial_\tau^4 u \\
& + \int_{-\infty}^{\tau} \phi(\tau - \tau') u(\tau') d\tau',
\end{aligned}
\tag{2}
$$
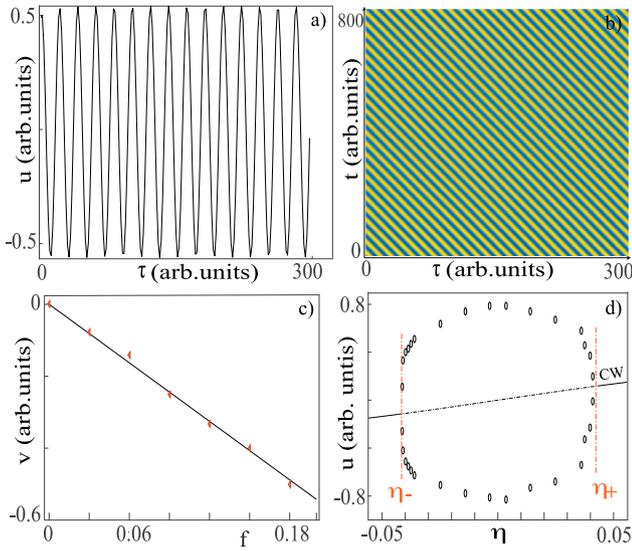
Fig. 2. Traveling wave solutions in the supercritical regime. (a) Profile of a periodic traveling wave solution obtained by numerical simulations of Eq. (2). (b) $t - \tau$ map showing the time evolution of the profile. (c) The velocity of the traveling wave solution v as a function of the strength of the Raman effect. Full line and red triangles show, respectively, the analytical solution (formula Eq. (5)) and numerical simulation results. (d) Supercritical bifurcation diagram obtained in the monostable regime. The full and broken lines correspond to the stable and unstable homogeneous steady state, respectively, while the circles correspond to the maxima and the minima of moving periodic structures. Parameters are $\beta = -1.5$, $\tau_0 = 14$, $f = 0.18$, $\tau_1 = 3$, $\tau_2 = 10$ (a, b, c) $\mu = -0.35$, and $\eta = -0.35$. (For interpretation of the references to color in this figure legend, the reader is referred to the web version of this article.)

A detailed derivation is presented in the Methods section. The parameters η and μ represent, respectively, the driven field and the frequency detuning deviations from their value at the critical point associated with bistability. The second and fourth-derivatives describe dispersion terms. The last contribution accounts for the stimulated Raman scattering with the new kernel function defined as $\phi(\tau) = \sqrt{3}/2af \exp^{-\tau_0(\tau-\tau')/\tau_2} \sin(\tau_0(\tau - \tau')/\tau_1)$ where f is the strength of the nonlocal delayed feedback.

The Fisher–Kolmogorov–Petrovsky–Piscunov (FKPP) equation derived in earlier research [37,39] is much different from Eq. (2). First, because the fourth derivative term originating from high-order dispersion is missing, the FKPP equation is unable to characterize the traveling modulational instability. Second, the scaling in fast and slow times utilized to derive the FKPP equation differs significantly from the scaling used to establish the Swift–Hohenberg with nonlocal response Eq. (2).

In the absence of stimulated Raman scattering, we recover the well-know SHE that has been first derived in the spatial domain [67,68] and in the temporal domain [66]. Without the fourth-order dispersion and the stimulated Raman scattering, Eq. (2) supports stationary localized structures and clusters of them both in the spatial domain [8] and in the temporal domain [66]. In this case, traveling wave instability and motion of temporal structures are forbidden. This is because, in the absence of stimulated Raman scattering and fourth order of dispersion, Eq. (2) is variational. This means that a Lyapunov functional exists for this equation, ensuring that the evolution will move towards the state, for which the functional has the smallest possible value that is compatible with the system boundary conditions.

The linear CW solutions of Eq. (2) satisfies the cubic equation $\eta = u_s^3 - (\mu + \sqrt{3}f/2)u_s = u_s^3 - 3\delta u_s/4$. The linear stability analysis with respect to finite frequency perturbations of the form $\exp(\lambda t + i\omega\tau)$ yields eigenvalues λ of the linear operator. The CWs states exhibit a traveling wave instability leading to moving periodic solutions when the real part of λ is positive. When taking into account the stimulated Raman scattering and higher order dispersion, a portion of homogeneous solutions

u_s undergo a traveling wave instability in the range $u_- < u_s < u_+$. The thresholds associated with this instability are

$$u_{\pm} = \pm\sqrt{\frac{\beta^2 + 4\mu}{3} - \frac{\sqrt{3}f(\tau_1^2 + \tau_2^2)}{3(\tau_1^2 - \tau_2^2)}}. \tag{3}$$

The corresponding injected field amplitudes are

$$\eta_{\pm} = -\left[\frac{\sqrt{3}f}{6}\frac{\tau_1^2}{\tau_1^2 - \tau_2^2} + \frac{5\sqrt{3}f + 8\mu - \beta}{12}\right]u_{\pm}, \tag{4}$$

where the frequency at both thresholds is $\omega_c^2 = -\beta/2$ with ω_c as the critical frequency. From this threshold emerge periodic traveling wave solutions whose profile and $t - \tau$ map are shown respectively, in Fig. 2(a) and 2(b). We derive an analytical formula for the velocity v of a traveling wave solution. The results are plotted in Fig. 2(c), showing excellent agreement between the analytical formula and numerical results. The bifurcation diagram is shown in Fig. 2(d) indicating that the traveling wave instabilities appear supercritically. The mathematical expressions for the traveling wave instability thresholds $\eta_{\pm}$ and the corresponding intracavity field amplitudes $u_{\pm}$ are provided explicitly in Methods section, respectively (see Eqs. (3) and (4)). The temporal period at both thresholds is $T_c = 2\pi\sqrt{2}/\sqrt{-\beta}$. We have also estimated the linear velocity of the periodic solution

$$v = \frac{\partial Im(\lambda)}{\partial\omega_c} = \frac{4\sqrt{3}f_r\beta\tau_0^3\tau_1^4\tau_2^4(\tau_1^2 + \tau_2^2)A_1}{A_2^2}, \tag{5}$$

where A_1 and A_2 are

$$
\begin{aligned}
A_1 &= [3\beta\tau_1^2\tau_2^2 - 4\tau_0^2(\tau_1^2 - \tau_2^2)] \\
&\quad - 4\tau_0^4(\tau_1^2 + \tau_2^2)^2, \\
A_2 &= \beta\tau_1^2\tau_2^2[\beta\tau_1^2\tau_2^2 - 4\tau_0^2(\tau_1^2 - \tau_2^2)] \\
&\quad + 4\tau_0^4(\tau_1^2 + \tau_2^2)^2.
\end{aligned} \tag{6}
$$

The velocity as well as the thresholds associated with the traveling wave instability have been obtained analytically within the limit of a low-frequency regime.

3. Isolas of frequency comb generation

In the absence of stimulated Raman scattering, the fourth-order dispersion strongly affects the dynamical behavior of all fiber resonators by allowing for new unstable frequencies to appear, and the modulational unstable domain to become bounded [63]. In the monostable case, the primary instability threshold is degenerate where two separate frequencies simultaneously appear while in the bistable case, high-frequency modulational instability precedes the limit point [63]. Furthermore, the fourth-order dispersion allows for the stabilization of dark LSs in the temporal [18] and spatial [69] domains. The interaction and pinning can be strongly modified by the influence of high-order dispersion effects [25,26].

Localized structures usually found close to the subcritical modulational instability [7,8] exhibit a well-known homoclinic snaking type of bifurcation that has been first reported in the time domain in [18], and in the spacial domain [69] (see also recent papers on this issue [70,71]). They exhibit multistability behavior in a finite range of parameters referred to as the pinning region [72]. From a dynamical point of view, their bifurcation diagram consists of two snaking curves; one describes LSs with odd number of peaks, the other corresponds to an even number of peaks. The two snaking curves are connected and emerge from the modulational instability threshold. They are intertwined, which is associated with the back-and-forth oscillations across the pinning region. This feature is a characteristic of systems possessing a reflection symmetry in the spatial domain $x \rightarrow -x$ or in the temporal domain ($\tau \rightarrow -\tau$) such as a Swift–Hohenberg type of equation [73,74] and the Lugiato–Lefever equation [70,71,75].
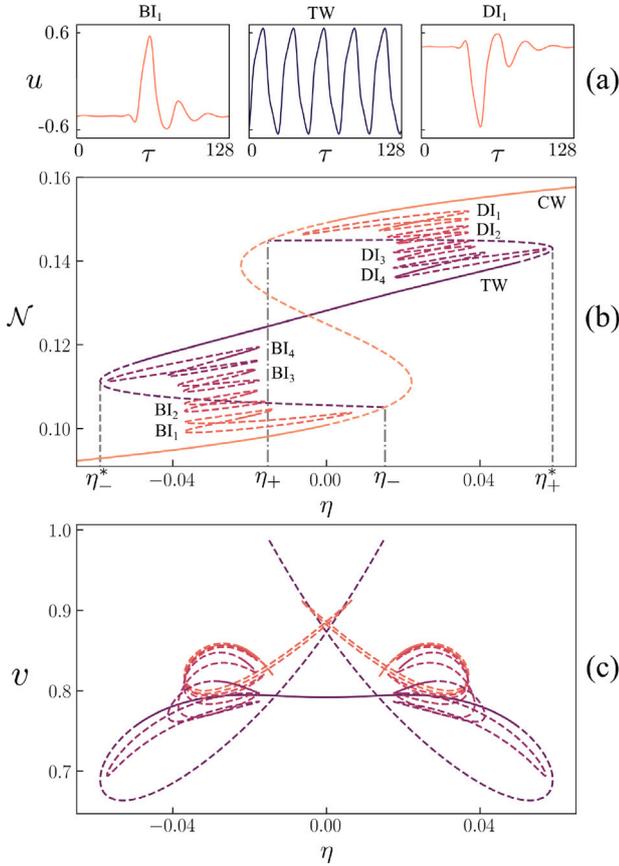
Fig. 3. Isola stack of localized structures obtained by continuation algorithm of Eq. (2). (a) Solution profiles for the respective points in the bifurcation diagram with $\eta = -0.015$, $\eta = 0.003$, and $\eta = +0.014$. (b) Bifurcation diagram obtained in the bistable regime. BI_n and DI_n, i=1,2,3,4 represent bright and dark isolas of solutions with n peaks and n dips, respectively. (c) Speed of LSs as a function of the injection parameter η. Parameters are $\mu = -0.1$, $\beta = -1.8$, $f = 0.28$, $\tau_0 = 1$, $\tau_1 = 3$, and $\tau_2 = 10$. (For interpretation of the references to color in this figure legend, the reader is referred to the web version of this article.)

3.1. Isolas of localized structures in the Swift–Hohenberg equation with nonlocal response

In what follows, we investigate numerically the formation of both bright and dark LSs under the combined influence of SRS-Kerr together with fourth-order dispersion. The presence of stimulated Raman scattering breaks the reflection symmetry and allows for the motion of LS. We focus on a strongly nonlinear regime where the traveling wave bifurcation is subcritical. For this purpose, we proceed by discretizing Eq. (2) in $N = 512$ nodes with a temporal step size of $\Delta \tau = 0.25$. Temporal derivatives with respect to the retarded time τ are then computed spectrally for better accuracy and time integration is performed using a 4th order adaptive Runge–Kutta scheme. traveling waves and moving bright and dark localized structures solutions of Eq. (2) are obtained by integrating numerically with periodic boundary conditions. They are shown in Fig. 3(a), and they are denoted by TW, BI_1, and DI_1, respectively.

We first seek moving periodic and localized states with constant speed v. These states correspond to solutions of Eq. (2) in the co-moving frame with v

$$0 = \eta + \mu u - u^3 + v\partial_\tau u + \beta \partial_\tau^2 u - \partial_\tau^4 u \tag{7}$$
$$+ \frac{\sqrt{3}}{2fa} \int_{-\infty}^{\tau} \phi(\tau - \tau')u(\tau')d\tau'.$$

In addition, due to the translational symmetry of the system, we must add a pinning condition in order to ensure the uniqueness of the solution

$$0 = \int u_0(\tau)\partial_\tau u(\tau)d\tau. \tag{8}$$

This condition can be derived by imposing that the difference with a previously known solution u_0 for a given parameter $\eta_0 \approx \eta$ must be minimized, i.e., $min_{\Delta\tau}\|D(\Delta\tau)\|$, where $\|.\|$ is the L_2 norm, which will be defined below, and $D(\Delta\tau) \equiv u(\tau + \Delta\tau) - u_0(\tau)$. Eqs. (7) and (8) are solved by means of the pseudo-arclength continuation method [76] which allows to seamlessly follow the solution branch through folds (cf. Fig. 3).

To visualize these solutions, it is convenient to plot the dimensionless L_2 norm,

$$\mathcal{N} = \int d\tau |u - u_s|^2 \tag{9}$$

as a function of η. The results are summarized in the bifurcation diagram shown in Fig. 3(b). The critical thresholds $\eta_\pm$ associated with the TW instability are located on the upper and lower branch of the CW solution.

In the bistable regime, the TW instability always appears subcritically. From the threshold associated with this instability emerges an unstable branch of TW periodic solutions (dotted purple curve). The existence domain of TW periodic solutions is in the range $\eta_-^* < \eta < \eta_+^*$ (purple curve). This branch of TW solutions is connected to the upper threshold η_+ by a dotted purple curve as shown in Fig. 3(b). More importantly, the left (right) portion of Fig. 3(b) shows a set of branches of bright (dark) LS. These localized state branches are distinguished by the multitude of peaks and dips in their temporal structure. An example of periodic TW wave, bright and dark localized structures are shown in Fig. 3(a). The two sets of branches of bright and dark LSs form isolas of localized states that are not connected to the thresholds of the TW instabilities. We estimate the velocity of LSs to better characterize them, and the results are presented in Fig. 3(c). This figure shows that the speed reduces as the number of peaks rises. The isola branch with the purple color corresponds to the single peak solution that is the fastest LSS.

Although both the bright and the dark localized branches of solutions are shown in the bifurcation diagram in Fig. 3, to simplify the analysis, we focus on the dark localized structures. Their shape changes as a function of the strength of the injected field amplitude as shown Fig. 4(a) for the corresponding points A, B, C, and D in the bifurcation diagram of Fig. 4(c). This figure is obtained by zooming in on Fig. 3(b) around the upper CW solution. This portion of the bifurcation diagram reveals clearly that branches of localized structures are not connected to the TW instability. Moving dark localized structures form single or multiple isolas. This feature is displayed in Fig. 4(c). The spectra of dark LS are shown in Fig. 4(b).

3.2. Isolas of localized structures in the generalized LLE with Raman scattering

The reduction from the generalized LLE Eq. (1) to a Swift–Hohenberg equation without a nonlocal delayed response Eq. (2) is a well-known framework for the analysis of periodic or localized structures [8]. It typically applies to systems that experience a modulational instability close to a second-order critical point, marking the onset of a hysteresis loop (nascent bistability). It has been demonstrated that the Swift–Hohenberg equation with high orders of dispersion and no Raman scattering reproduces qualitatively the same results as the full LLE model [66].

In what follows, we shall show that isolas of localized structures are also solutions of the full LLE model Eq. (1). For this purpose, let us fix the detuning parameter by considering the monostable regime, i.e., $\Delta < \sqrt{3}$. Fig. 5 depicts an example of a single peak moving localized structures and their corresponding comb.
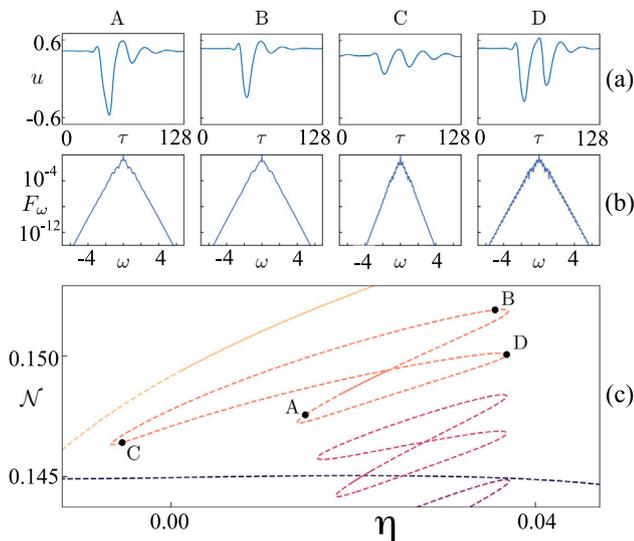
Fig. 4. (a) Solution profiles corresponding to the points A, B, C and D in the bifurcation diagram. (b) Corresponding Fourier spectra. (c) Magnification on the upper CW branch of the bifurcation diagram presented in Fig. 3(b). Same parameters as in Fig. 3. (For interpretation of the references to color in this figure legend, the reader is referred to the web version of this article.)

They are obtained numerically by using a periodic boundary condition compatible with the ring geometry of the optical resonator depicted in Fig. 1. The grid size is 512 with a temporal step size of 0.25.

The T-ζ map of Fig. 5(a) depicts traveling temporal localized structures with a constant speed. The motion is directly imputable to the stimulated Raman scattering effect since it breaks the reflection symmetry $\zeta \to -\zeta$. As shown in Fig. 5(b), the profile of temporal localized structures becomes asymmetric in this case. The spectral content of the intensity profile forms an optical frequency comb that shows an asymmetry as shown in Fig. 5(c). The comb lines are all equally spaced since the free spectral range, given by the inverse of the cavity round-trip time, has a fixed value.

Fig. 6 depicts a single peak localized structure (BI_1), bounded states (BI_2), and a periodic train of peaks (TW) moving at constant speed. The above mentioned continuation algorithm allows for the construction of the bifurcation diagram shown in Fig. 6(b). There are four curves in the plot of the L_2 norm as a function of the injected field E_i. The blue curve displays a single CW solution. The red curve represents the branch of traveling periodic solutions that emerges from the CW solutions. The green and orange curves represent the single and bound branches, which state localized structures with one and two peaks, respectively. Because they are far apart, temporal localized structures interact via their exponentially decaying tails and bounded states. Interactions of localized structure have been studied in the absence of stimulated Raman scattering, in the spatial domain [77]. This weak type of interaction is affected by the third- [25] and the fourth- [26] orders of dispersion.

The profile of a moving peak localized structure is deeply affected by the change of the injected field amplitude. This feature is illustrated in Fig. 7(a). A zoom on that figure shows that neither branches of single and bounded states localized are connected to the CW solutions (see Fig. 7(b)). As in the limit of nascent bistability where the dynamics is governed by a Swift–Hohenberg with nonlocal delayed feedback (Eq. (2)), the generalized LLE Eq. (1) exhibits isola type of solutions. The stimulated Raman scattering is directly responsible for disconnecting the localized branches of solutions from the CW solution. Because we integrate the nonlocal delayed integral term from $-\infty$ to a finite time, the reflection symmetry is broken. However, the branches of periodic TW solutions are still connected to the CW solutions.
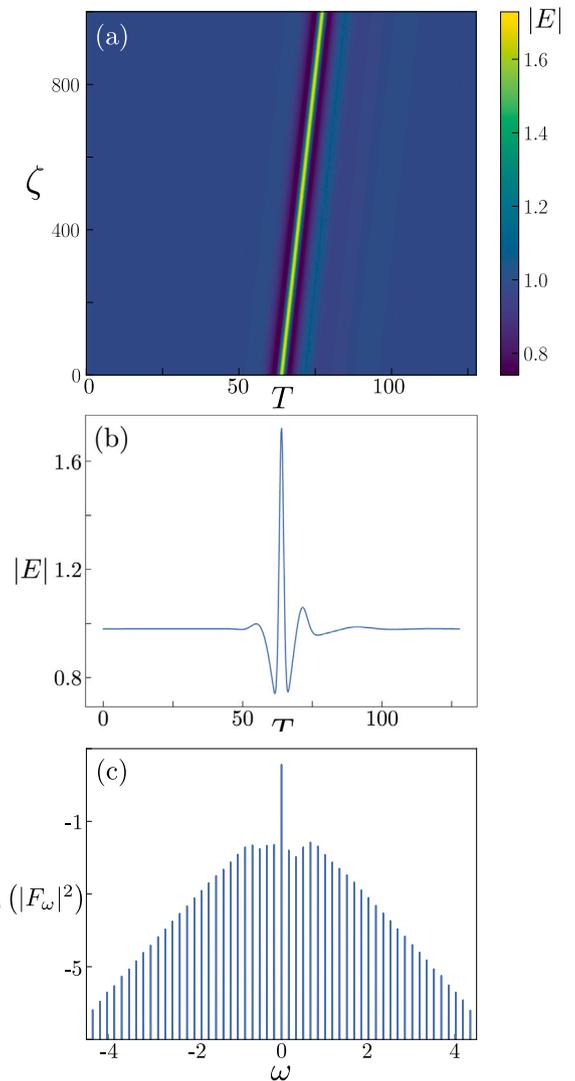
Fig. 5. Moving localized structures obtained by numerical simulations of Eq. (1). (a) T-ζ map. (b) Temporal profile (c) Corresponding Fourier spectrum. Parameters are $\Delta = 1.7$, $E_i = 1.219$, $f_r = 0.05$, $\beta_2 = 1$, $\beta_4 = 0.01$, $\tau_0 = 1$, $\tau_1 = 3$, $\tau_2 = 10$. Numerical simulation has been performed using 512 cells, with a T step of 0.25 and a ζ step of 0.001.

In order to better understand the creation of isolas from the perspective of dynamical system theory, we give a geometrical explanation in the next section.

4. Geometrical interpretation

The localized states are stationary solutions of the co-moving frame of Eq. (2). Geometrically, these solutions correspond to homoclinic curves in the phase portrait [78]. The latter is a geometrical representation of the trajectories of the dynamical system of Eq. (2) in the phase plane, which is the Poincaré plane (see Fig. 8). The geometrical interpretation of homoclinic snaking is a well-documented issue and is by now fairly well understood [74]. The homoclinic orbit bifurcates from a heteroclinic loop which is generated by connecting CW (equilibrium) to a periodic orbit. The homoclinic curves correspond to the asymptotic state of the localized solutions and are formed by the intersection of the stable (W^s) and unstable (W^u) manifolds of the uniform equilibrium. The phase portrait's manifold intersection is shown schematically in Fig. 8. The points represent the various localized states or homoclinic curves. Note that the equilibrium that produces manifolds is a hyperbolic equilibrium for the related stationary system and corresponds to
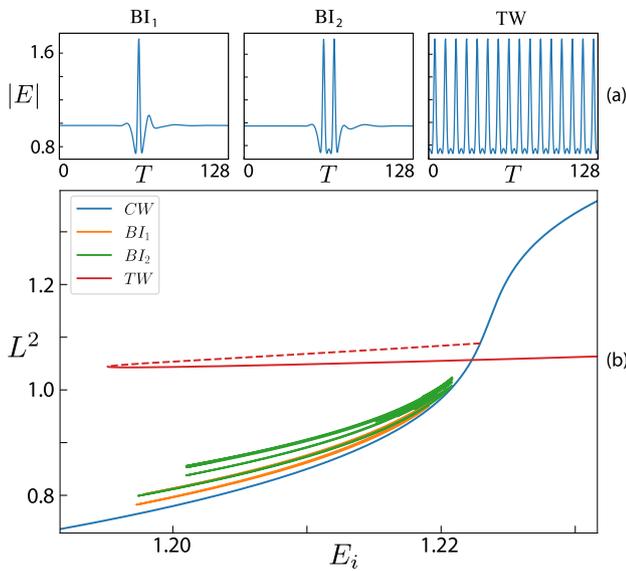
Fig. 6. (a) Temporal profile of a single, bounded states, and periodic train of pulses indicated by BI_1, BI_2, and TW, respectively. (b) Bifurcation diagram representing CW (blue curve), train of periodic pulses (red curve) solutions. The unstable branch of TW is indicated in doted curve. The two isolas of localized structures are indicated by green and orange colors, respectively. Parameters are the same as in Fig. 5. (For interpretation of the references to color in this figure legend, the reader is referred to the web version of this article.)

a uniform stable condition of the spatiotemporal system (co-mobile). That is, the manifolds are the nonlinear extension of the eigenvectors associated with the equilibrium.

When the phase portrait's dimension is higher than two, the manifolds surrounding a hyperbolic point exhibit a complicated geometric structure typically referred to as *manifold entanglement* [79,80]. Poincaré first proposed that this entanglement would lead to chaotic behavior in regular temporal systems [81]. The coexistence of localized structures caused by the entangled manifolds in the portrait space of stationary systems is known as the homoclinic snaking bifurcation diagram [74,82]. This coexistence of solutions is characterized by the fact that the symmetrical localized states are connected with other ones with more or less one spatial oscillation. This process occurs through saddle–node bifurcations, generating a snake-like structure in the bifurcation diagram [74]. Experimental observation of this bifurcation diagram has been carried out for a liquid crystal light valve with optical feedback [83]. The ordered sequence of homoclinic curves (localized states) results from spatial reflection symmetry in the system ($\tau \to -\tau$), where Π represents the spatial reflection symmetry plane.

Then the unstable manifold intercepts the plane of symmetry Π. Due to the reflection symmetry, the stable manifold intercepts Π in a mirror image. This entanglement generates a sequence of symmetric localized states represented by the green dots in Fig. 8(a). The bifurcation diagram associated with LSs contains two intertwined snaking curves. This classical scenario is not expected in irreversible systems, i.e., systems devoid of reflection symmetry. In this case, asymmetrical solutions shown in Fig. 3(a) or in Fig. 8(b) are possible. Fig. 8(b) illustrates asymmetrical solutions indicated by black points. These are close to the homoclinic bifurcation diagram, but not connected with other LSs. This behavior is referred to as *isolas* [84–88]. Namely, the solutions only connect with other four asymmetric ones, forming a loop in the phase diagram, typically with the shape of a Lissajous curve (see Figs. 3 and 4(c)).

In the case that the system under study loses reflection symmetry ($\tau \not\to -\tau$), the intersection of the stable and unstable manifolds does not coincide generically with the surface Π that initially accounted for the plane of symmetry [89]. Even both manifolds now are not symmetrical.
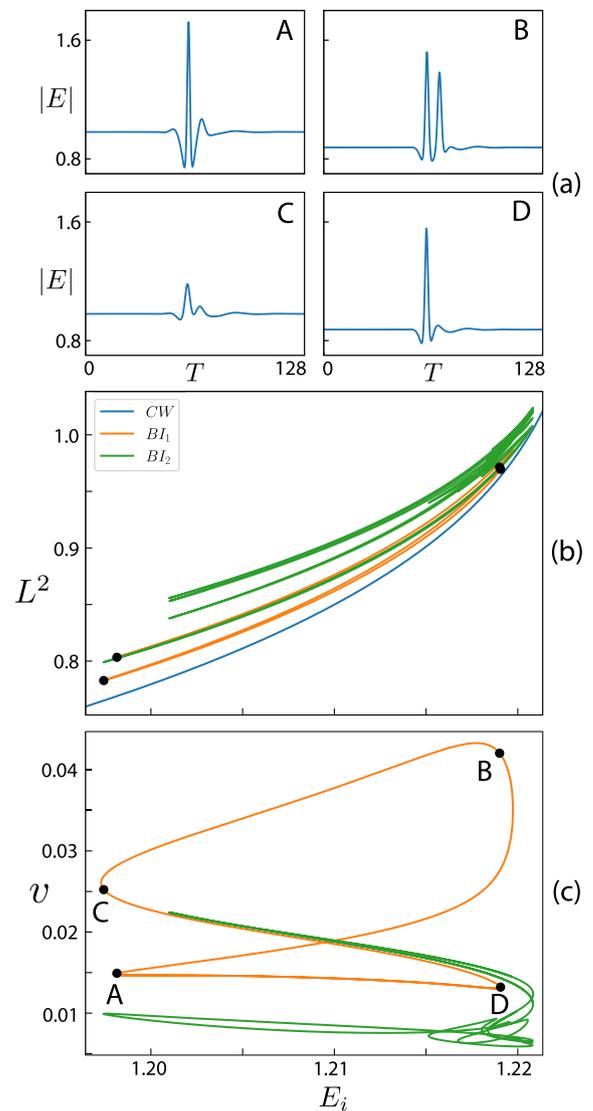
Fig. 7. (a) Profiles of localized structures at different values of the injected field intensity. (b) Zoom of Fig. 6(b) showing isola of solutions for the generalized LLE Eq. (1). (c) Speed of the localized structures as a function of the injected field intensity. Parameters are the same as in Fig. 6. (For interpretation of the references to color in this figure legend, the reader is referred to the web version of this article.)
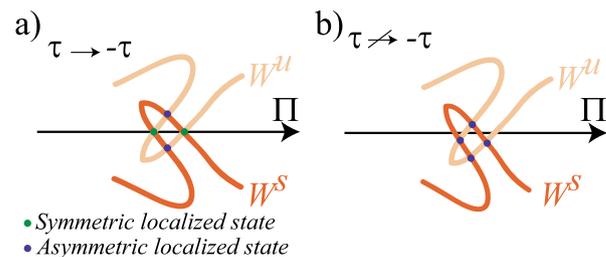
Fig. 8. Schematic representation of stable (W^s) and unstable (W^u) manifold in the phase portrait. Representation of intersection of stable and unstable manifolds in systems with reflection symmetry (a) and without symmetry (b). Π accounts for the spatial reflection symmetry plane. The colored dots represent the homoclinic curves (localized structures). (For interpretation of the references to color in this figure legend, the reader is referred to the web version of this article.)

Fig. 8(b) depicts the typical image of the intercepts of manifolds in systems without reflection symmetry. Then all localized structures become asymmetric since there is no ordered sequence imposed by reflection

symmetry. Hence, the system transforms the homoclinic snaking into an isola stack (see Fig. 3) [86,87,89]. Namely the localized structures in the bifurcation diagram are connected by groups of four solutions generically.

In brief, the Swift–Hohenberg Eq. (2) without the effect of stimulated Raman scattering is known to exhibit a homoclinic snaking bifurcation diagram [89]. When taking into account the odd-order of dispersion, the reflexion symmetry is broken. For instance, in the presence of third-order dispersion, bright and dark dissipative solitons become asymmetric and acquire an additional group velocity shift associated with this asymmetry [90]. In this case, isolas of localized structures have been reported [90]. Incorporating the stimulated Raman scattering breaks the reflection symmetry and induces an isola stack. In this case, the homoclinic snaking bifurcation structure breaks up.

5. Conclusions

To sum up, we have investigated the confinement of light in driven nonlinear ring cavities containing a micro-structured photonic crystal fiber. The effects of the Kerr effect, stimulated Raman scattering, and high orders of dispersion on the formation of temporal localized structures have been theoretically examined. In the spectrum domain, these nonlinear solutions correspond to combs.

We performed a real order parameter description leading to the derivation of a Swift–Hohenberg type of equation with a nonlocal delayed response. Due to the presence of stimulated Raman scattering, the resultant Swift–Hohenberg equation is nonvariational, which means that there is no potential or Lyapunov functional to minimize. We show that this equation supports traveling waves solutions. We have characterized them in the supercritical regime. The threshold as well as the speed are estimated.

In the subcritical regime where periodic traveling solutions coexist with stable background (CW solution), both bright and dark moving localized structures are stabilized. These structures are asymmetric and direct numerical simulations have indicated that both structures have an overlapping domain of coexistence. By using a continuation algorithm, we have established their bifurcation diagram and estimated their velocity. More importantly, the stimulated Raman scattering breaks the reflection symmetry and destroys the homoclinic snaking bifurcation structure, allowing for isola stacks of dark localized states to form. This is in contrast with reversible systems that possess the reflection symmetry where the bifurcation diagram consists of two intertwined snaking curves.

The full LLE has been numerically simulated to demonstrate proof of isolas branches of solutions. As a function of the injected field strength, single peak and bounded states of localized branches of solutions have been constructed. Note that there have been reports of other type of localized structures with varying width [37,39,40]. These solutions arise from front interaction, need bistability between CWs for their formation, and exhibit a collapsed snaking type of bifurcation in their bifurcation structure. Contrastingly, the localized states described here are distinct in a number of ways: they have a finite size determined by the frequency that is the most unstable; their formation does not necessitate bistability; and their bifurcation diagram exhibits behavior akin to an isola stack. Finally, we have provided a geometrical interpretation of the impact of broken reflection symmetry mediated by the stimulated Raman scattering on the formation of isola stacks.

Declaration of competing interest

The authors declare that they have no known competing financial interests or personal relationships that could have appeared to influence the work reported in this paper.

Data availability

Data will be made available on request.

Compliance with ethics requirements

This article does not contain any studies with human or animal subjects.

Appendix

A.1. Derivation of the Swift–Hohenberg equation with delayed nonlocal response

The purpose of this section is to present the derivation of a Swift–Hohenberg with a delayed nonlocal response, i.e., the stimulated Raman scattering. To do that, we explore the fast-slow time dynamics of the generalized LLE Eq. (1), in the neighborhood of the critical point associated with nascent bistability. At this second-order critical point that marks the onset of a hysteresis loop, the output versus input characteristics have an infinite slope, i.e., $\partial E_i/\partial|E_s| = \partial^2 E_i/\partial|E_s|^2 = 0$ where $|E_s|$ is the CW solutions of Eq. (1) that satisfy $E_i^2 = |E_s|^2[1+(\Delta-|E_s|^2)^2]$. The coordinates of the critical point associated with bistability are [45]

$$E_c = (3 - i\sqrt{3})\frac{E_{ic}}{4}, \quad E_{ic}^2 = \frac{8\sqrt{3}}{9}, \quad \text{and } \Delta_c = \sqrt{3}. \tag{10}$$

To explore the vicinity of the second-order critical point, we define a small parameter ϵ which measures the distance from the critical point associated with the bistability as

$$\Delta = \Delta_c + \delta\epsilon^2. \tag{11}$$

We then expand the input field amplitude, and the slowly varying intracavity electric field in terms of ϵ as

$$E_i = E_{ic} + s_1\epsilon + s_2\epsilon^2 + s\epsilon^3 + \cdots, \tag{12}$$

$$E = E_c + \epsilon(u_0, v_0) + \epsilon^2(u_1, v_1) \tag{13}$$
$$+ \epsilon^3(u_2, v_2) + \cdots$$

where u_i and v_i denote the real and the imaginary parts of the intracavity field. Our goal is to derive a slow time and slow space amplitude equation. A preliminary analysis indicates that we need to consider a small second-order dispersion coefficient $\beta_2 \equiv \epsilon\beta$ to have bounded solutions in both slow and fast time. We seek corrections to the steady states at criticality that depend on slow variables $t = \epsilon^2\zeta$ and $\tau = 3^{1/4}\epsilon T$. We assume in addition that the strength of the delayed Raman effect is small, i.e., $f_r \to f\epsilon^2$, and we set the β_4 value to one. Replacing the above expansions in the generalized Lugiato–Lefever Eq. (1), we obtain at the leading order in ϵ: $s_1 = 0$ and $u_0 = \sqrt{3}v_0$. At the next order ϵ^2, we obtain $s_2 = \sqrt{\delta/2\sqrt{3}}$. Finally at ϵ^3, we get

$$\frac{\partial u_0}{\partial t} = s + \left(\frac{\delta}{\sqrt{3}} - \frac{2f}{3}\right)u_0 - \frac{4}{3\sqrt{3}}u_0^3 \tag{14}$$

M. Tlidi et al.

Chaos, Solitons and Fractals: the interdisciplinary journal of Nonlinear Science, and Nonequilibrium and Complex Phenomena 174 (2023) 113808

$$+ \frac{\beta}{\sqrt{3}} \frac{\partial^2 u_0}{\partial \tau^2} - \frac{1}{\sqrt{3}} \frac{\partial^4 u_0}{\partial \tau^4}$$
$$+ \frac{2af}{3} \int_{-\infty}^{\tau} e^{-\frac{\tau_0(\tau-\tau')}{\tau_2}}$$
$$\sin\left[\tau_0(\tau-\tau')/\tau_1\right] u_0(\tau') d\tau',$$

With the following changes of parameters $t \rightarrow 3^{3/2} t/4$, $\eta = (3^{3/2}/4)s$, $\mu = \sqrt{3}(\sqrt{3}\delta - 2f)/4$, and $\beta \rightarrow 3/4\beta$, we obtain the Swift–Hohenberg equation with stimulated Raman scattering Eq. (2), where the new kernel function is defined as $\phi(\tau) = \sqrt{3}/2af \exp^{-\tau_0(\tau-\tau')/\tau_2} \sin(\tau_0(\tau - \tau')/\tau_1)$.

References

[1] Jones DJ, Diddams SA, Ranka JK, Stentz A, Windeler RS, Hall JL, et al. Carrier-envelope phase control of femtosecond mode-locked lasers and direct optical frequency synthesis. Science 2000;288:635.

[2] Udem T, Holzwarth R, Hänsch TW. Optical frequency metrology. Nature 2002;416:233.

[3] Fortier T, Baumann E. 20 Years of developments in optical frequency comb technology and applications. Commun Phys 2019;2:1.

[4] Picqué N, Hänsch TW. Frequency comb spectroscopy. Nature Photon 2019;13:146.

[5] Herr T, Brasch V, Jost JD, Wang CY, Kondratiev NM, Gorodetsky ML, et al. Temporal solitons in optical microresonators. Nature Photon 2014;8:145.

[6] Kippenberg TJ, Gaeta AL, Lipson M, Gorodetsky ML. Dissipative Kerr solitons in optical microresonators. Science 2018;361:6402.

[7] Scroggie AJ, Firth WJ, McDonald GS, Tlidi M, Lefever R, Lugiato LA. Pattern formation in a passive Kerr cavity. Chaos Solitons Fractals 1994;4:1323.

[8] Tlidi M, Mandel P, Lefever R. Localized structures and localized patterns in optical bistability. Phys Rev Lett 1994;73:640.

[9] Nozaki K, Bekki N. Low-dimensional chaos in a driven damped nonlinear Schrödinger equation. Physica D 1986;21:381.

[10] Wabnitz S. Suppression of interactions in a phase-locked soliton optical memory. Opt Lett 1993;18:601.

[11] Matsko AB, Savchenkov AA, Liang W, Ilchenko VS, Seidel D, Maleki L. Mode-locked Kerr frequency combs. Opt Lett 2011;36:2845.

[12] Coen S, Randle HG, Sylvestre T, Erkintalo M. Modeling of octave-spanning Kerr frequency combs using a generalized mean-field Lugiato–Lefever model. Opt Lett 2013;38:37.

[13] Lugiato LA, Prati F, Gorodetsky M, Kippenberg TJ. From the Lugiato–Lefever equation to microresonator-based soliton Kerr frequency combs. Phil Trans R Soc A 2018;376:20180113.

[14] Bao H, Olivier L, Rowley M, Chu ST, Little BE, Morandotti R, et al. Turing patterns in a fiber laser with a nested microresonator: Robust and controllable microcomb generation. Phys Rev Res 2020;2:023395.

[15] Soto-Crespo JM, Akhmediev N, Grelu P, Belhache F. Quantized separations of phase-locked soliton pairs in fiber lasers. Opt Lett 2003;28:1757.

[16] Olivier M, Roy V, Piché M. Third-order dispersion and bound states of pulses in a fiber laser. Opt Lett 2006;31:580.

[17] Berrios-Caro E, Clerc MG, Leon AO. Flaming 2π kinks in parametrically driven systems. Phys Rev E 2016;94:052217.

[18] Tlidi M, Gelens L. High-order dispersion stabilizes dark dissipative solitons in all-fiber cavities. Opt Lett 2010;35:306.

[19] Tlidi M, Bahloul L, Cherbi L, Hariz A, Coulibaly S. Drift of dark cavity solitons in a photonic-crystal fiber resonator. Phys Rev A 2013;88:035802.

[20] Milian C, Skryabin DV. Soliton families and resonant radiation in a micro-ring resonator near zero group-velocity dispersion. Opt Express 2014;22:3732.

[21] Bahloul L, Cherbi L, Hariz A, Tlidi M. Temporal localized structures in photonic crystal fibre resonators and their spontaneous symmetry-breaking instability. Phil Trans R Soc A 2014;372:20140020.

[22] Turaev D, Vladimirov AG, Zelik S. Long-range interaction and synchronization of oscillating dissipative solitons. Phys Rev Lett 2012;108:263906.

[23] Akhmediev N, Karlsson M. Cherenkov radiation emitted by solitons in optical fibers. Phys Rev A 1995;51:2602.

[24] Skryabin DV, Gorbach AV. Colloquium: Looking at a soliton through the prism of optical supercontinuum. Rev Modern Phys 2010;82:1287.

[25] Vladimirov AG, Gurevich SV, Tlidi M. Effect of Cherenkov radiation on localized-state interaction. Phys Rev A 2018;97:013816.

[26] Vladimirov AG, Tlidi M, Taki M. Dissipative soliton interaction in Kerr resonators with high-order dispersion. Phys Rev A 2021;103:063505.

[27] Brasch V, Geiselmann M, Herr T, Lihachev G, Pfeiffer MHP, Gorodetsky ML, et al. Photonic chip–based optical frequency comb using soliton Cherenkov radiation. Science 2016;351:357.

[28] Spillane SM, Kippenberg TJ, Vahala KJ. Ultralow-threshold Raman laser using a spherical dielectric microcavity. Nature 2002;415:621.

[29] Lin G, Coillet A, Chembo YK. Nonlinear photonics with high- whispering-gallery-mode resonators. Adv Opt Photonics 2017;9:828.

[30] Min B, Yang L, Vahala K. Controlled transition between parametric and Raman oscillations in ultrahigh-Q silica toroidal microcavities. Appl Phys Lett 2005;87:181109.

[31] Liang W, Ilchenko V, Savchenkov A, Matsko A, Seidel D, Maleki L. Passively mode-locked Raman laser. Phys Rev Lett 2010;105:143903.

[32] Karpov M, Guo H, Kordts A, Brasch V, Pfeiffer MHP, Zervas M, et al. Raman self-frequency shift of dissipative Kerr solitons in an optical microresonator. Phys Rev Lett 2016;116:103902.

[33] Liu X, Sun C, Xiong B, Wang L, Wang J, Han Y, et al. Integrated high-Q crystalline AlN microresonators for broadband Kerr and Raman frequency combs. ACS Photonics 2018;5:1943.

[34] Chen-Jinnai A, Kato T, Fujii S, Nagano T, Kobatake T, Tanabe T. Broad bandwidth third-harmonic generation via four-wave mixing and stimulated Raman scattering in a microcavity. Opt Express 2016;24:26322.

[35] Zhu S, Shi L, Ren L, Zhao Y, Jiang B, Xiao B, Zhang X. Controllable Kerr and Raman-Kerr frequency combs in functionalized microsphere resonators. Nanophotonics 2019;8:2321.

[36] Cherenkov AV, Kondratiev NM, Lobanov VE, Shitikov AE, Skryabin DV, Gorodetsky ML. Raman-Kerr frequency combs in microresonators with normal dispersion. Opt Express 2017;25:31148.

[37] Clerc MG, Coulibaly S, Tlidi M. Time-delayed nonlocal response inducing traveling temporal localized structures. Phys Rev Res 2020;2:013024.

[38] Yao S, Bao C, Wang P, Yang C. Generation of stable and breathing flat-top solitons via Raman assisted four wave mixing in microresonators. Phys Rev A 2020;101:023833.

[39] Clerc MG, Coulibaly S, Parra-Rivas P, Tlidi M. Non-local Raman response in Kerr resonators: Moving temporal localized structures and bifurcation structure. Chaos 2020;30:083111.

[40] Parra-Rivas P, Coulibaly S, Clerc MG, Tlidi M. Influence of stimulated Raman scattering on Kerr domain walls and localized structures. Phys Rev A 2021;103:013507.

[41] Coen S, Tlidi M, Emplit P, Haelterman M. Convection versus dispersion in optical bistability. Phys Rev Lett 1999;83:2328.

[42] Odent V, Tlidi M, Clerc MG, Glorieux P, Louvergneaux E. Experimental observation of front propagation in a negatively diffractive inhomogeneous Kerr cavity. Phys Rev A 2014;90. 011806(R).

[43] Xue X, Xuan Y, Liu Y, Wang P-H, Chen S, Wang J, et al. Mode-locked dark pulse Kerr combs in normal-dispersion microresonators. Nat Photon 2015;9:594.

[44] Garbin B, Wang Y, Murdoch SG, Oppo G-L, Coen S, Erkintalo M. Experimental and numerical investigations of switching wave dynamics in a normally dispersive fibre ring resonator. Eur Phys J D 2017;71:240.

[45] Lugiato LA, Lefever R. Spatial dissipative structures in passive optical systems. Phys Rev Lett 1987;58:2209.

[46] Parra-Rivas P, Knobloch E, Gomila D, Gelens L. Dark solitons in the Lugiato–Lefever equation with normal dispersion. Phys Rev A 2016;93:063839.

[47] Parra-Rivas P, Gomila D, Knobloch E, Coen S, Gelens L. Origin and stability of dark pulse Kerr combs in normal dispersion resonators. Opt Lett 2016;41:2402.

[48] Kostet B, Gopalakrishnan S, Averlant E, Soupart Y, Panajotov K, Tlidi M. Vectorial dark dissipative solitons in Kerr resonators. OSA Continuum 2021;4:1564.

[49] Kostet B, Soupart Y, Panajotov K, Tlidi M. Coexistence of dark vector soliton Kerr combs in normal dispersion resonators. Phys Rev A 2021;104:053530.

[50] Yulin AV, Skryabin DV, J. Russell P St. Four-wave mixing of linear waves and solitons in fibers with higher-order dispersion. Opt Lett 2004;29:2411.

[51] Demircan A, Bandelow U. Supercontinuum generation by the modulation instability. Opt Commun 2005;244:181.

[52] Dudley JM, Genty G, Coen S. Supercontinuum generation in photonic crystal fiber. Rev Modern Phys 2006;78:1135.

[53] Dudley JM, Taylor JR, editors. Supercontinuum generation in optical fibers. Cambridge University Press; 2010.

[54] Milian C, Gorbach AV, Taki M, Yulin AV, Skryabin DV. Solitons and frequency combs in silica microring resonators: Interplay of the Raman and higher-order dispersion effects. Phys Rev A 2015;92:033851.

[55] Chembo YK, Grudinin IS, Yu N. Spatiotemporal dynamics of Kerr-Raman optical frequency combs. Phys Rev A 2015;92:043818.

[56] Lin G, Chembo YK. Phase-locking transition in Raman combs generated with whispering gallery mode resonators. Opt Lett 2016;41:3718.

[57] Cherenkov AV, Kondratiev N, Lobanov V, Shitikov A, Skryabin D, Gorodetsky M. Raman-Kerr frequency combs in microresonators with normal dispersion. Opt Express 2017;25:31148.

[58] Liu K, Yao S, Yang C. Raman pure quartic solitons in Kerr microresonators. Opt Lett 2021;46:993.

[59] Liu M, Huang H, Lu Z, Wang Y, Cai Y, Zhao W. Dynamics of dark breathers and Raman-Kerr frequency combs influenced by high-order dispersion. Opt Express 2021;29:18095.

[60] Liu M, Huang H, Lu Z, Zhou W, Wang Y, Cai Y, et al. Stimulated Raman scattering induced dark pulse and microcomb generation in the mid-infrared. New J Phys 2022;24:053003.

[61] Blow KJ, Wood D. Theoretical description of transient stimulated Raman scattering in optical fibers. IEEE J Quantum Electron 1989;25:2665.

[62] Lin Q, Agrawal GP. Raman response function for silica fibers. Opt Lett 2006;31:3086.

[63] Tlidi M, Mussot A, Louvergneaux E, Kozyreff K, Vladimirov AG, Taki M. Control and removal of modulational instabilities in low-dispersion photonic crystal fiber cavities. Opt Lett 2007;32:662.

[64] Parra-Rivas P, Gomila D, Gelens L. Coexistence of stable dark- and bright-soliton Kerr combs in normal-dispersion resonators. Phys Rev A 2017;95:053863.

[65] Vladimirov AG, Gurevich SV, Tlidi M. Effect of cherenkov radiation on localized-state interaction. Phys Rev A 2018;97:013816.

[66] Hariz A, Bahloul L, Cherbi L, Panajotov K, Clerc M, Ferré MA, et al. Swift-Hohenberg equation with third-order dispersion for optical fiber resonators. Phys Rev A 2019;100:023816.

[67] Mandel P, Georgiou M, Erneux T. Transverse effects in coherently driven nonlinear cavities. Phys Rev A 1992;46:4252.

[68] Tlidi M, Georgiou M, Mandel P. Transverse patterns in nascent optical bistability. Phys Rev A 1993;48:4605.

[69] Tlidi M, Kockaert P, Gelens L. Dark localized structures in a cavity filled with a left-handed material. Phys Rev A 2011;84:013807.

[70] Parra-Rivas P, Gomila D, Matías MA, Coen S, Gelens L. Dynamics of localized and patterned structures in the Lugiato–Lefever equation determine the stability and shape of optical frequency combs. Phys Rev A 2014;89:043813.

[71] Parra-Rivas P, Knobloch E, Gelens L, Gomila D. Origin, bifurcation structure and stability of localized states in Kerr dispersive optical cavities. IMA J Appl Math 2021;86:856.

[72] Pomeau Y. Front motion, metastability and subcritical bifurcations in hydrodynamics. Physica D 1986;23:3.

[73] Champneys AR. Homoclinic orbits in reversible systems and their applications in mechanics, fluids and optics. Physica D 1998;112:158.

[74] Woods PD, Champneys AR. Heteroclinic tangles and homoclinic snaking in the unfolding of a degenerate reversible Hamiltonian Hopf bifurcation. Physica D 1999;129:147.

[75] Gomila D, Scroggie AJ, Firth WJ. Bifurcation structure of dissipative solitons. Physica D 2007;227:70.

[76] Keller HB. Numerical solution of bifurcation and nonlinear eigenvalue problem. In: Application of bifurcation theory. Academic Press; 1977.

[77] Vladimirov AG, McSloy JM, Skryabin DV, Firth WJ. Two-dimensional clusters of solitary structures in driven optical cavities. Phys Rev E 2002;65:046606.

[78] Coullet P. Localized patterns and fronts in nonequilibrium systems. Int J Bifurcation Chaos 2002;12:2445.

[79] Jackson EA. Perspectives of nonlinear dynamics: Volume 1. Cambridge: Cambridge University Press; 1989.

[80] Wiggins S. Normally hyperbolic invariant manifolds in dynamical systems. Springer Science & Business Media; 1994.

[81] Poincaré H. Les Methodes Nouvelles de la Mecanique Celeste. Vol. III, Paris, 1899 reprint. New York: Dover; 1957.

[82] Coullet P, Riera C, Tresser C. Stable static localized structures in one dimension. Phys Rev Lett 2000;84:3069.

[83] Haudin F, Rojas RG, Bortolozzo U, Residori S, Clerc MG. Homoclinic snaking of localized patterns in a spatially forced system. Phys Rev Lett 2011;107:264101.

[84] Wadee MK, Coman CD, Bassom AP. Solitary wave interaction phenomena in a strut buckling model incorporating restabilisation. Physica D 2002;163:26.

[85] Beck M, Knobloch J, Lloyd DJ, Sandstede B, Wagenknecht T. Snakes, ladders, and isolas of localized patterns. SIAM J Math Anal 2009;41:936.

[86] Knobloch J, Lloyd DJ, Sandstede B, Wagenknecht T. Isolas of 2-pulse solutions in homoclinic snaking scenarios. J Dynam Differential Equations 23:93, 52011.

[87] Makrides E, Sandstede B. Predicting the bifurcation structure of localized snaking patterns. Physica D 2014;268:59.

[88] Nishiura Y, Watanabe T. Traveling pulses with oscillatory tails, figure-eight-like stack of isolas, and dynamics in heterogeneous media. Physica D 2022;440:133448.

[89] Burke J, Houghton SM, Knobloch E. Swift-Hohenberg equation with broken reflection symmetry. Phys Rev E 2009;80:036202.

[90] Parra-Rivas P, Gomila D, Leo F, Coen S, Gelens L. Third-order chromatic dispersion stabilizes Kerr frequency combs. Opt Lett 2014;39:2971.